Outgassing of CO_2 dominates in the coastal upwelling off the northwest African coast

Nathalie Lefèvre [a],[*], Doris Veleda [b], Susan E. Hartman [c]

[a] IRD, Sorbonne Universités (UPMC, Univ Paris 06) - CNRS-IRD-MNHN, LOCEAN Laboratory, 4 place Jussieu, 75005, Paris, France
[b] Department of Oceanography, DOCEAN, Federal University of Pernambuco, Recife, Brazil
[c] National Oceanography Centre, European Way, Southampton, SO14 3ZH, UK

A B S T R A C T

The Eastern Boundary Upwelling System off northwest Africa is among the most productive regions of the ocean. In 2019, two merchant ships equipped with an underway CO_2 system sampled the region following exactly the same track from 10°N to 36°N. We determine the sources and sinks of CO_2 and the seasonal cycle along the track. A weak permanent upwelling (WPU), a permanent upwelling (PU) and an open ocean regions are identified. The WPU (26°N to 33°N) is a source of CO_2 in summer and autumn, and a sink of CO_2 in winter and spring. Thermodynamic warming and cooling processes mainly drive the CO_2 variations in this region. The PU (20°N to 26°N) is a sink of CO_2 in spring and a source of CO_2 in other seasons. This region is the most productive and exhibits the largest variability of the CO_2 flux. The supply of CO_2 from subsurface waters dominate over the carbon uptake by biology, which leads to a strong outgassing, especially in winter and autumn. A sink of CO_2 occurs in spring only in the PU. Near Cape Blanc (20°N) in July 2019, a source of CO_2 is observed around 20°N within $\pm 1°$ of latitude and becomes a sink of CO_2 a few days later when the ship samples back the same area. South of 18°N, out of the influence of the coastal upwelling, the region is a sink of CO_2 in winter only and the region is mainly controlled by physical processes. Using voyages from 2010 to 2022, seawater fCO_2 significantly increases at a rate ranging from 1.82 µatm yr^{-1} to 2.10 µatm yr^{-1} close to the atmospheric increase. This is associated with a pH decrease between 0.0016 and 0.0022 yr^{-1}. Nevertheless, there is no clear trend of the CO_2 flux in any region.

1. Introduction

The four Eastern Boundary Upwelling Systems (EBUS), California, Humboldt, Canary and Benguela upwelling systems, are highly productive regions despite their small areas (<1% of the ocean), sustaining major fisheries (1995). They are important for biogeochemical cycles as upwelled water are enriched in nutrients and supersaturated with respect to atmospheric CO_2. The Canary Current Upwelling System (CCUS), extending from the Iberian peninsula to Guinea, 43°N to 8°N, is the second most productive EBUS (Carr, 2001; Demarcq and Somoue, 2015) and with the small pelagic fish resources that continue to increase (Failler, 2020). From 10°N to the Strait of Gibraltar (36°N), the upwelling presents different characteristics along the coast of Africa depending on the wind forcing and the shape of the coast (Pelegrí and Peña-Izquierdo, 2015). The variability of the upwelling along the coast and the nutrient concentrations explain the large regional differences in productivity (Arístegui et al., 2009). With the wind blowing alongshore along the coast of Africa, the surface water moves offshore and subsurface water upwells, supplying nutrients and CO_2-rich waters to the surface ocean. The input of nutrients leads to strong biological activity, which decreases the CO_2 content of surface waters. The two mechanisms are antagonistic and whether eastern boundary upwelling systems are sinks or sources of CO_2 is unclear (Kämpf and Chapman, 2016b).

Based mainly on upwelling features, Wooster (1976) identified seasonal upwelling from January through May in the 12°N-20°N region, strong upwelling throughout the year between 20°N and 25°N and strongest upwelling from June through October between 25°N-43°N. Although the boundaries of the regions vary slightly, several studies identified three main subregions (e.g. Arístegui et al., 2009; Cropper et al., 2014; Lathuilière et al., 2008; Mittelstaedt, 1983). From 10°N to 19°N, a weak seasonal coastal upwelling occurs in winter-spring. In the northern region, from the Canary islands to the Strait of Gibraltar, the

upwelling occurs year-round, is weak in winter-spring and intense in summer-fall (Pelegrí and Benazzouz, 2015). From 21°N to 26°N the coastal upwelling is also permanent and more intense in summer, but it is stronger than from 26°N to 35°N (Cropper et al., 2014; Diogoul et al., 2021). The stronger intensity in summer is associated with the seasonal migration of the trade winds (Cropper et al., 2014). The 19°N-21°N latitudinal band is a transition zone between the seasonal coastal upwelling and the permanent coastal upwelling zones.

At interannual timescales, the North Atlantic Oscillation (NAO) and the East Atlantic (EA) patterns are the main drivers of the CCUS variability (Bonino et al., 2019; Georg et al., 2022; Gómez-Letona et al., 2017). The NAO intensifies (weakens) the winds and upwelling in its positive (negative) phase. The EA is similar to the NAO and consists of a north-south dipole, southeastward to the NAO. Both climate indices can act isolated or connected, intensifying or weakening the effects of winds and upwelling in the CCUS region.

The strong productivity of the coastal upwelling is visible from space as depicted by high chlorophyll concentrations. For the CCUS, Lathuilière et al. (2008) describe the surface chlorophyll distribution using satellite observations from SeaWiFS (Sea-viewing Wide Field-of-View Sensor) from 2000 to 2004. They report different patterns of chlorophyll concentrations in roughly the same three subregions defined as subtropical gyre (24°N to 33°N), inter-gyre (19°N-24°N) and recirculation gyre 10°N to 19°N. In the subtropical gyre, the chlorophyll is low, confined to the coast and presents a weak seasonal cycle. In contrast, the inter-gyre region off Cape Blanc shows the maximum offshore extension of chlorophyll with the highest concentrations. Bonino et al. (2021) showed that the upwelling seasonality in the CCUS drives the offshore organic carbon variability hundreds of kilometers from the coast through cross-shore redistribution of production. Using chlorophyll data provided by Copernicus Marine Environmental Monitoring Service (CMEMS), Siemer et al. (2021) detected a decrease of chlorophyll concentrations in the weak permanent upwelling, between 26°N and 33°N, and in the permanent upwelling, between 20°N and 26°N, from 1998 to 2018.

There are not many estimates of the air-sea CO_2 flux for the Atlantic coastal upwelling systems. Along the Iberian coast, Borges and Frankignoulle (2002) found net sinks of CO_2 for the atmosphere in summer, during the upwelling season, in the Galician upwelling system (42°N-43°N). In the Mauritanian-Cap Vert upwelling region, González-Dávila et al. (2017) found an increase of CO_2 outgassing due to upwelling intensification between 2005 and 2012. Further north, the region of the Canary Current, from 28°N to 36°N, is a sink of CO_2 in winter and a source in summer 2019, mainly controlled by thermodynamic variations (Curbelo-Hernández et al., 2021). EBUS are complex and variable systems, which makes their source or sink of CO_2 status unclear. Thus, the central and northern Chile is a source of CO_2 (e.g. Torres et al., 2002) while the Benguela system south of 20°S is a sink of CO_2 (e.g. Gregor and Monteiro, 2013; Monteiro, 2010; Santana-Casiano et al., 2009).

In addition to the seasonal source or sink patterns of coastal upwellings, the evolution of the air-sea CO_2 flux over time is unclear. Using a regional ocean model, Lachkar and Gruber (2013) made sensitivity simulations under increased upwelling-favorable winds. In particular, they examined the biological response and its impact on the air-sea CO_2 flux. They found that, under upwelling intensification, CO_2 would increase over time due to reduced biological efficiency of carbon uptake in the southern Canary Current system near Cape Blanc. In contrast, they found a large increase in production compensating the upwelling driven CO_2 outgassing in the central and northern Canary Current system. They attributed these different responses to the different nutrient limitation states and to factors controlling biological growth. Similarly, Lachkar (2014) made sensitivity simulations in the California and in the Canary current systems to examine the effect of upwelling intensification on ocean acidification based on the volume of water undersaturated in aragonite. He found that doubling CO_2 concentration and wind stress

would offset each other so that the volume of aragonite-undersaturated water did not change much. These sensitivity studies highlight the complexity of predicting the evolution of air-sea CO_2 flux in EBUS.

Data obtained by Voluntary Observing Ships (VOS) provide high frequency surface ocean measurements generally on repeat routes. Many such routes are offshore of the upwelling regions and/or exhibit some longitudinal variability, which makes it difficult to determine the behavior of the coastal upwelling zones. As they are highly dynamic regions, addressing whether they are sources or sinks of CO_2 requires high resolution CO_2 monitoring within the same area. However, in 2019, the *Cap San Lorenzo* (the France to Brazil VOS) sailed closer to the African coast in the 10°N-36°N region and repeated exactly the same track, crossing the weak and permanent upwelling areas. The *M/V Maersk Raleigh* (a UK to Falklands VOS) also sampled the region on the same track in January 2019 and completes the dataset. The objectives of this study are to determine the seasonal cycle, the drivers of the CO_2 variability, and to estimate the sources and sinks of CO_2 along the track. In addition, we selected observations collected from 2010 to 2021 to detect any trend of the CO_2 flux.

2. Materials and methods

2.1. Study area

The study area covers the region from 10°N to 36°N. We have selected the VOS cruises that sail most closely to the African coast and that follow the same track over time (in red on Fig. 1). The ship sails from the Strait of Gibraltar (36°N), east of the Canary Islands and east of the Cape Verde Arquipelago. Siemer et al. (2021) identified three productive upwelling regions (the Permanent Upwelling PU, the Cap Juby Weak Permanent Upwelling, CJWPU, and the Cape Ghir Weak Permanent Upwelling CGWPU) indicated in black on the map. The colored background gives the mean chlorophyll concentration provided by the Copernicus Marine Environmental Monitoring Service (CMEMS). The main surface currents are indicated in white.

The coastal surface circulation is dominated by the Portugal current (PC), the Canary Current (CC) and the Mauritanian Current (MC). The PC and CC flow southward along the coast. Near 20°N, the CC detaches from the coast and feeds the westward North Equatorial Current (NEC). Between 5°N and 10°N, the North Equatorial Counter Current (NECC) flows eastward, across the Atlantic, from the American coast to the African coast. When it reaches the African coast, part of the NECC flows northwards forming the MC (e.g. Arístegui et al., 2009; Pelegrí and Peña-Izquierdo, 2015). In January, February, and April to December 2019, the ships sample the CGWPU and the CJWPU.

Two main water masses feed the nutrient-rich upwelling ecosystem: the North Atlantic Central Water (NACW) and the South Atlantic Central Water (SACW). From 20°N off the coast of Africa to the Cape Verde Islands, the Cape Verde frontal zone constitutes the boundary between the NACW and the SACW (Pastor et al., 2015). The NACW is saltier than the SACW and both water masses exhibit a large range of temperatures and salinity. The origin of the eastern NACW and SACW are located around 20°W-35°W, 39°N-48°N and 0°E-15°E, 30°S-40°S respectively (Liu and Tanhua, 2021).

2.2. In situ and satellite data

The *Cap San Lorenzo* merchant ship sailing from France to Brazil has been equipped with an underway CO_2 system from General Oceanics to monitor the surface fugacity of CO_2 in the ocean and in the atmosphere. The fugacity of CO_2 (fCO_2) takes into account the non-ideal behavior of CO_2 gas. It differs numerically by a few micro-atmospheres from the partial pressure of CO_2 (pCO_2) so we often confuse them. Measurements have started in 2008 and are averaged every 5 min. The description of the CO_2 system, based on infrared detection, and the data processing are described by Pierrot et al. (2009). A wet box including a shower-head
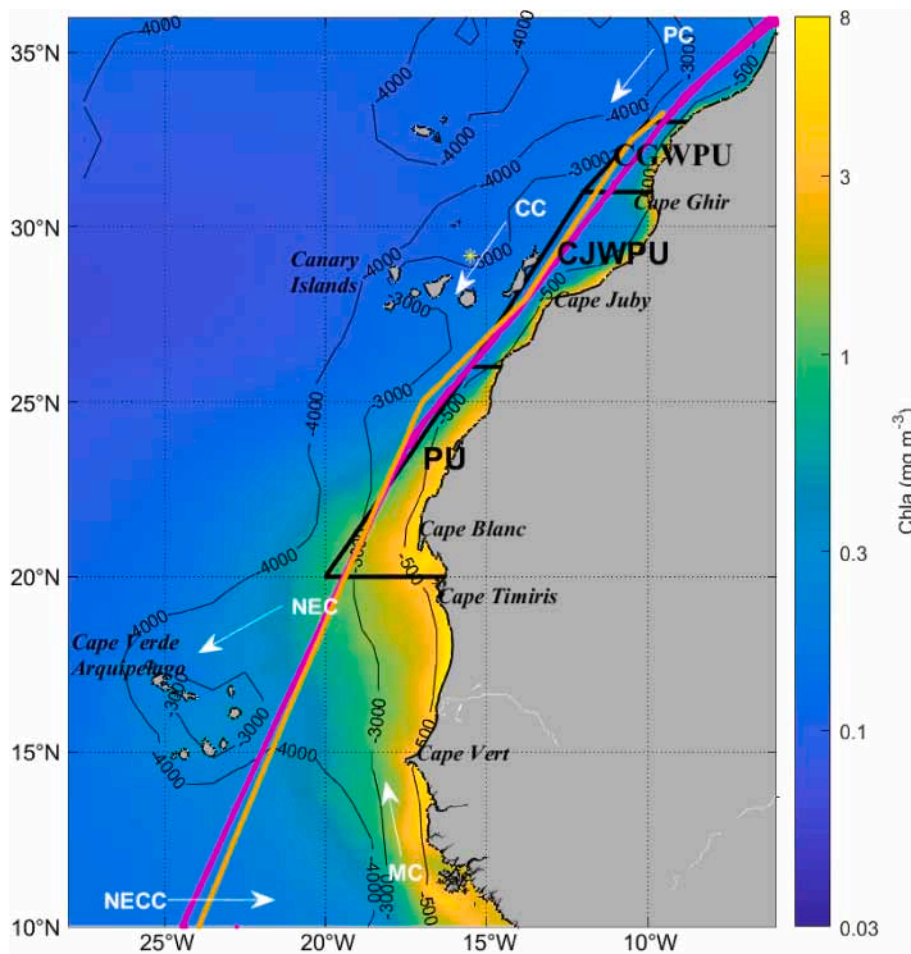
Fig. 1. Map of the study area with the tracks of the Cap San Lorenzo for the voyages of 2019 (in magenta) and of the Maersk Raleigh in January 2019 (in orange). The main surface currents (in white, PC Portugal Current, CC Canary Current, MC Mauritanian Current, NEC North Equatorial Current, and NECC North Equatorial Counter Current) are superimposed on the year-round chlorophyll concentration averaged over 1998–2020. The black contour lines indicate the isobaths 500 m, 3000 and 4000 m. The polygon boxes close to the African coast correspond to the Permanent Upwelling (PU), the Cape Juby Weak Permanent Upwelling (CJWPU) and the Cape Ghir Weak Permanent Upwelling (CGWPU) zones defined by Siemer et al. (2021). The European Station for Time-Series in the Ocean of the Canary Islands (ESTOC) (Llinas et al., 1994; Santana-Casiano and González-Dávila, 2015) is also indicated (yellow star).

equilibrator is installed in the engine room of the ship. The dry box is installed near the wet box and includes a non-dispersive infrared analyser (Li-7000 by LICOR®). Three standard gases with known concentrations of CO_2 and a zero-gas (nitrogen) are run every 3 h to calibrate the detector that measures the molar fraction of CO_2 (xCO_2). The ship is also equipped with a thermosalinograph to measure sea surface temperature (SST) and salinity (SSS) underway.

fCO_2 was measured on the *MV Raleigh Fisher* (formally *Maersk Raleigh*) using duplicate Pro-Oceanus CV sensors with a gas permeable interface and a non-dispersive infrared detector CO_2 analyser. The gas stream circulating in the closed measurement loop equilibrates with the sample and then is measured by the detector. This means that the raw readings are the mole fraction of CO_2 in wet air at the tank temperature. The system is described by Jiang et al. (2014).

To maintain the factory calibration an automatic zero-point calibration (AZPC) is applied every 6 h, where the gas stream is routed through CO_2 absorbent to provide a zero ppm CO_2 measurement.

There are various processing steps for the carbon dioxide data similar for both systems and described in details by Pierrot et al. (2009). Initially, the raw CO_2 values for each sensor are adjusted for differences between the temperature they were measured at and the sea surface temperature. These values are then used together with the pressure measurement to calculate pCO_2. The internal humidity sensor is used in conversion to dry measurements and the amount of CO_2 dissolved in the seawater is calculated by taking into account the solubility coefficient (that depends on temperature in situ and salinity (Weiss, 1974),). The final conversion to fCO_2 uses the atmospheric pressure.

Additionally, daily water samples were collected on board the *MV Raleigh Fisher* to validate the measurements of conductivity and the

measurements of pCO_2 (by calculation of pCO_2 from measurements of Total Alkalinity (TA), by titration, and Total Dissolved Inorganic Carbon, by coulometry, made on the water sample using a Vindta, Versatile Instrument for the Determination of total inorganic carbon and Total Alkalinity, at the National Oceanography Centre). Precision and accuracy for replicate analyses was better than ± 4.0 µmol kg^{-1} and ± 3.9 µmol kg^{-1} for DIC and TA respectively.

The fCO_2 data are archived in the SOCAT database (www.socat.info).

Seawater samples were taken during several PIRATA (Prediction and Research moored Array in the Tropical Atlantic) cruises in the Atlantic, from 2005 to 2019, for TA analyses. The cruises covered the region 10°N-36°N, east of 35°W. The samples were analyzed using a closed-cell potentiometric titration method by Edmond (1970). The system was calibrated by the Certified Reference Material distributed by Prof. A. Dickson (Scripps Institution of Oceanography, San Diego, CA, USA). The accuracy of TA was estimated at ± 3 µmol kg^{-1}.

The chlorophyll concentrations come from the Copernicus Marine Environmental Monitoring Service (CMEMS) website (https://resources.marine.copernicus.eu, http://marine.copernicus.eu/documents/QUID/CMEMS-OC-QUID-009-030-032-033-037-081-082-083-085-086-098.pdf, level 4 product OCEANCOLOUR_GLO_CHL_L4_REP_OBSERVATIONS_009_082). The monthly product at 4 km resolution is chosen to provide the biological conditions of the region. Different sensors (SeaWiFS, MODIS-Aqua, MERIS, VIIRS and OLCI-S3A) are used to produce the chlorophyll observations, which eliminates the data gaps that often occur with the products taken from one sensor only. Chlorophyll data are collocated along the track of the ship by taking the closest chlorophyll pixel to the geographical position of the ship. Monthly chlorophyll data are taken at the representative month of the ship

observations. Then, in order to compare chlorophyll concentrations with in situ data, all datasets are binned by 0.25° of latitude along the track of the ship from 10°N to 36°N.

The 6-hourly wind speeds, at 0.25° spatial resolution, from the cross-calibrated multi-platform version 2 (CCMP2 Wentz et al., 2015) are averaged monthly and are used to calculate the sea-air CO_2 flux.

Satellite SST and SSS are compared to observations by collocating the satellite data along the cruise tracks. The SST comes from the MODIS (Moderate-Resolution Imaging Spectrometer) Aqua on a 4 km grid. The sea surface salinity fields are 18-day Gaussian means from SMOS (Soil Moisture and Ocean Salinity Satellite) at a resolution of 25 km (CATDS CEC LOCEAN debias V4.0, doi: 10.17882/52804).

2.3. Calculation of the CO_2 flux and carbon parameters

The flux of CO_2 across the sea-air interface is calculated according to the following formula:

$$F = k * So * (fCO_{2\ sw} - fCO_{2\ atm}) \qquad (1)$$

where k is the gas exchange coefficient of Wanninkhof (2014), parameterized as a function of wind speed U and Sc is the Schmidt number, a function of temperature:

$$k = 0.251 <U^2> (Sc/660)^{-0.5} \qquad (2)$$

So is the solubility of CO_2 in seawater of Weiss (1974) and fCO_{2sw} and fCO_{2atm} are the surface fugacity of CO_2 in the ocean and in the atmosphere respectively. The atmospheric fCO_2 (fCO_{2atm}) recorded by the ship is compared to the fCO_{2atm} calculated using the monthly molar fraction of CO_2, xCO_2, recorded at the atmospheric station, Izaña, Tenerife, (28.31°N, 16.50°W).

An empirical total alkalinity-salinity relationship has been developed for the region 10°N-36°N, east of 35°W, using 124 seawater samples collected from 2005 to 2019 during PIRATA cruises (Lefèvre et al., 2021):

$$TA = 60.07\ (\pm1.24) * SSS + 201.51\ (\pm45.13),\ r^2 = 0.95 \qquad (3)$$

Equation (3) gives a RMSE (Root Mean Square Error) for TA of ±6.3 μmol kg^{-1}. For comparison, the more global relationship of Lee et al. (2006) gives a RMSE of ±8.5 μmol kg^{-1}.

Total inorganic carbon (TCO_2) and pH are calculated using SST, SSS, fCO_2 and TA, estimated by equation (3), and the CO2SYS program for Matlab (Sharp et al., 2020) using the dissociation constants of Mehrbach et al. (1973) refitted by Dickson and Millero (1987).

2.4. Calculation of thermal versus non-thermal processes on fCO_2

We estimate the relative importance of thermal (T) over non-thermal processes (B) following the method of Takahashi et al. (2002). The temperature effect is removed by calculating the fCO_2 normalized to the mean annual temperature T_{mean}:

$$fCO_2\_T_{mean} = fCO_2\ \exp[0.0423*(T_{mean} - SST)] \qquad (4)$$

The seasonal range of variations of fCO_2 normalized to T_{mean} is attributed to other processes than thermodynamics, such as biology or mixing. The effect of temperature is calculated by the difference between the mean and observed temperatures applied to the mean fCO_2 ($fCO_{2\ mean}$):

$$fCO_2\_therm = fCO_{2\ mean}\ \exp[0.0423*(SST - T_{mean})] \qquad (5)$$

The seasonal range of variations of fCO_2_therm represents the variations of fCO_2 caused by surface warming or cooling. The T/B ratio gives the relative importance of thermal over non-thermal processes:

$$T/B = [(fCO_2\_T_{mean})_{max} - (fCO_2\_T_{mean})_{min}] / [(fCO_2\_therm)_{max} - (fCO_2\_therm)_{min}] \qquad (6)$$

Values of T/B higher than 1 indicate that temperature effects dominate over biological and mixing processes.

2.5. Statistical and data analyses

The difference between two groups of data is assessed using a *t*-test if the distribution follows a normal law. If not, a non-parametric test is used instead. The non-parametric test of Mann-Whitney-U test is used to determine whether two groups come from the same distribution by testing if the medians are equal. The tests are performed with Matlab. Some of the cruises are outside the polygons defining the coastal upwelling area, especially in the permanent upwelling zone near 22°N-26°N where the ship further offshore (Fig. 1). In the following, the permanent upwelling zone is considered to include all the voyages of 2019 between 20°N and 26°N. The Mann-Whitney-U test show that the monthly means of fCO_2 between 20°N and 26°N are statistically similar to those located exactly in the permanent upwelling zone. The monthly means of MODIS SST and SMOS SSS in the upwelling polygons are not significantly different (two-sample *t*-test for normal distributions or Wilcoxon rank sum test) from the monthly means of the SST and SSS of the *Cap San Lorenzo* calculated for the same latitudinal band. Therefore, the voyages of the *Cap San Lorenzo* are considered as representative of the upwelling areas CGWPU, CJWPU and PU.

The seasonal distributions of fCO_2, SST and SSS are for the year 2019 when the *Cap San Lorenzo* sampled the area at nine different months. In January 2019, the data from the *Maersk Raleigh* complete the dataset. Only the months of March and June 2019 are missing. As shown by previous studies (e.g. Park and Wanninkhof, 2012), the seasonal cycle of fCO_2 and SST can be well represented with a harmonic fit of the form:

$$X = a + b\ \sin\ (2\ \pi\ mo/12) + c\ \cos\ (2\ \pi\ mo/12) \qquad (7)$$

where mo is the month varying between 1 (January) and 12 (December), and a, b and c are the fitting coefficients. The fit is determined using all the 2019 voyages in the 26-33°N, 20°N-26°N and 10°N-18°N regions. The a, b, c coefficients are given in Table S1.

The evolution of seawater fCO_2 over time is examined by calculating fCO_2 anomalies using all the voyages of the France-Brazil line that sampled the same regions as the ones studied for the year 2019. They consist of cruises sailing east of the Canary Islands and east of the Cape Verde Arquipelago made by the *Rio Blanco*, the *Santa Cruz* and the *Cap San Lorenzo*. For the selected cruises, the observations range from 2010 to 2022. A seasonal cycle is calculated using monthly averaged data from 2010 to 2022 in each region. Monthly anomalies are then calculated by subtracting this seasonal cycle to the monthly observations over the 2010–2022 period. The trend is calculated by linear regression on the monthly anomalies.

3. Results

3.1. Seasonal variability along the ship track in 2019

In order to describe the seasonal cycle along the ship track, we focus on the year 2019, as data are available almost every month during that year. Fig. 2 shows the comparison between the data collected from 2010 to 2022, excluding those in 2019, and the observations collected in 2019 grouped by month. No anomaly is detected in 2019. The data of 2019 are generally close to the median, which suggests that 2019 may be considered as a typical year to determine the seasonal cycle in this region.

Using all the voyages of 2019 between 10°N and 36°N, the molar fraction of CO_2 in the atmosphere averages 410.4 ± 3.2 ppm and compares well with the mean xCO_2 value of 411.1 ± 2.2 ppm at the Izaña atmospheric station in 2019. The minimum values are observed in September–October whereas the maximum values are in April–May. The conversion of xCO_2 to fCO_2 gives a mean value of atmospheric fCO_2 of
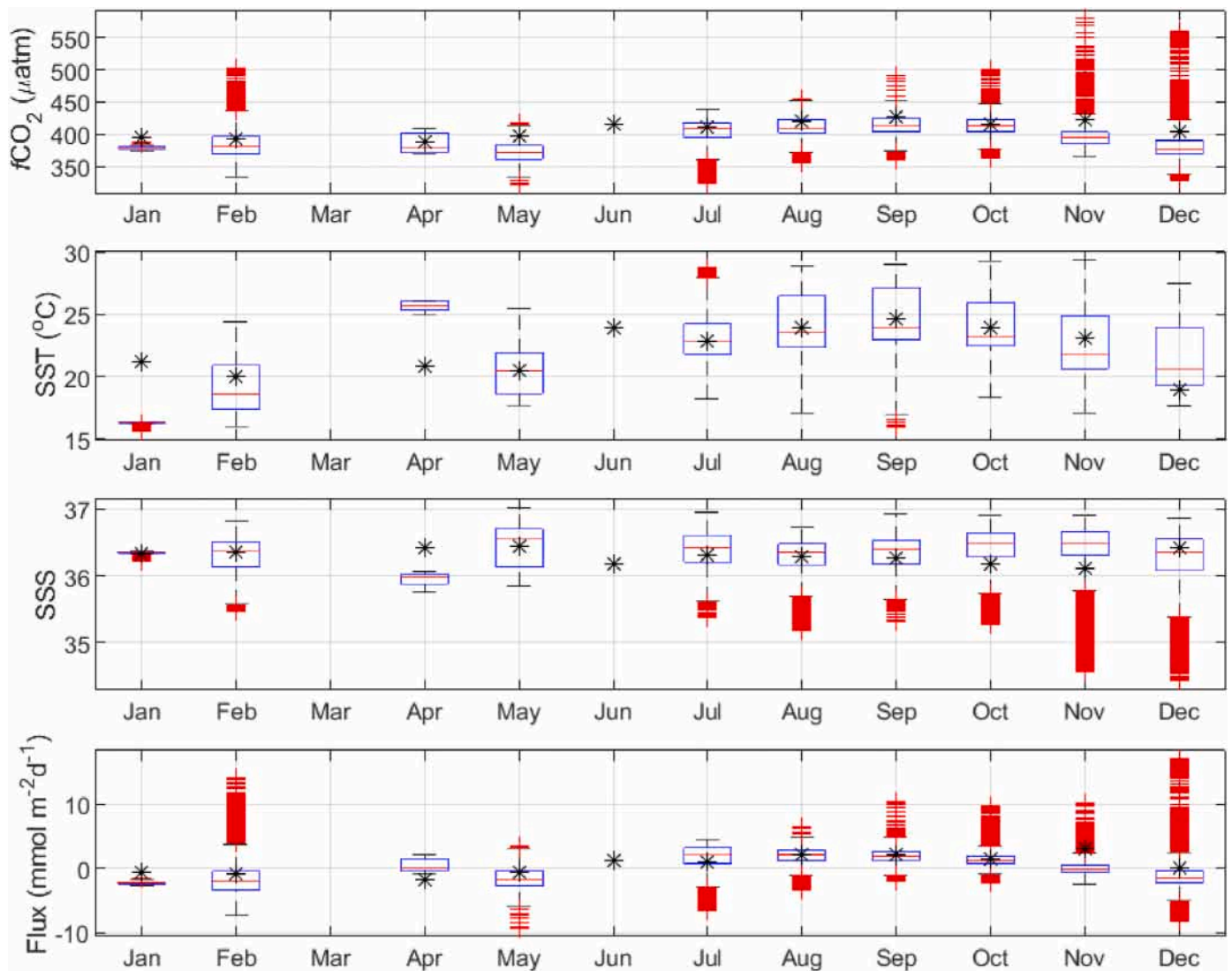
Fig. 2. Distribution of fCO$_2$, SST, SSS and CO$_2$ flux grouped by month using all the observations from 2010 to 2022 except 2019. The central mark of the box corresponds to the median with the bottom and top edges of the box indicating the 25th and 75th percentiles. The whiskers extend to the extreme data points and the red pluses are considered as outliers. The black stars are the observations of the year 2019.

398.1 ± 4.9 µatm for the voyages of the *Cap San Lorenzo* made in 2019. Using all the voyages along the VOS line from 10°N to 36°N, including those sailing further offshore the African coast, we calculate an atmospheric fCO$_2$ increase of 2.53 ± 0.07 µatm yr^{-1} over the 2010–2022 period.

The variations of seawater fCO$_2$, SST and SSS along the track of the *Cap San Lorenzo* are plotted from 10°N to 36°N for each season of 2019 (Fig. 3).

The representative month of each voyage is given in Table 1.

Overall, the seawater fCO$_2$ is very variable during each season (Fig. 3a-d). The highest fCO$_2$ values (>550 µatm) occur in the upwelling zone from 20°N to 26°N in winter and autumn (Fig. 3a and d) with the maximum value reaching 634 µatm in November 2019. The lowest fCO$_2$ values are in summer, in the same upwelling zone, with the lowest fCO$_2$ of 242 µatm measured in July 2019 (Fig. 3c). In contrast, the regions from 26°N to 33°N exhibit much lower variability with fCO$_2$ values ranging from 350 µatm in summer to 440 µatm in autumn 2019. On average, seawater fCO$_2$ below the mean atmospheric fCO$_2$ are observed in winter and spring (381 and 390 µatm, respectively) and increase towards summer and autumn (409 and 406 µatm, respectively). In the south, from 10°N to 18°N, the amplitude of fCO$_2$ variations is about 90

µatm, which is similar to the north, but the lowest fCO$_2$ occurs in winter and the highest in summer, whereas in the north, the lowest fCO$_2$ is in summer and the highest in autumn. South of 20°N, the ship sails further offshore (isobaths >3000 m) and samples surface waters outside the coastal upwelling region.

The SST decreases steeply from 10°N to 20°N. A smaller amplitude of SST variations is observed from 20°N to 36°N throughout the year (Fig. 3e-h). In each season, from 10°N to 20°N, the SST amplitude is over 5 °C and is significantly warmer than in the northern part of the transect. Overall, the surface water is significantly warmer in summer and autumn (>23 °C averaged over 10-36°N) than in winter and spring (<21.5 °C). From 20°N northward, the SST fluctuates by about 2–3 °C but does not present a strong decreasing trend as in the southern part. From 26°N to 33°N, SST gradually increases from winter to autumn with a mean SST of 18.48 ± 0.78 °C to 21.62 ± 1.22 °C respectively.

Surface waters are usually fresher south of 20°N than north of it. In spring and summer 2019, pronounced increase of SSS near 20°N-21°N is observed (Fig. 3j and k) usually over 0.5 but it reaches 1 in May–June with SSS varying from 36 to 37 (Fig. 3j). In the 10°N-18°N region, the mean SSS is lower than 36 in autumn and winter and lower than 36.2 in summer and spring. After the SSS increase near 20°N, SSS usually
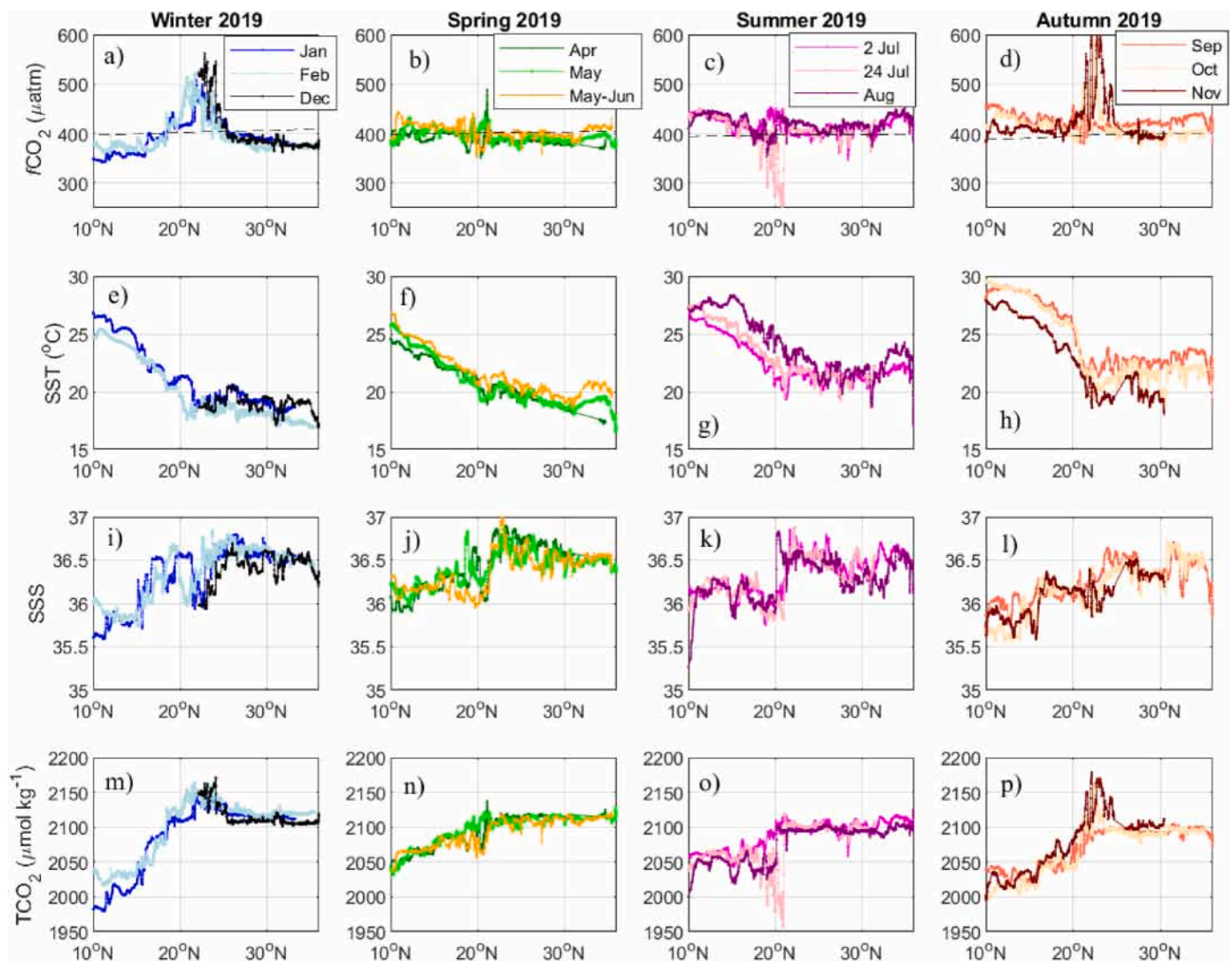
Fig. 3. Variations of fCO₂, SST, SSS and TCO₂, along the Cap San Lorenzo track and Maersk Raleigh, from 10°N to 36°N in winter, spring, summer and autumn 2019. Winter corresponds to December, January and February, spring to March, April, May, summer to June, July, August and autumn to September, October, and November. The dashed line (in panels a, b, c, d) corresponds to the mean atmospheric fCO₂ value for the season.

remains over 36.4 north of 26°N at each season (Fig. 3i–l).

At each season, TCO₂ concentrations are lower from 10°N to 20°N than north of 20°N (Fig. 3m to p). Near 20°N, TCO₂ concentrations vary strongly with lower values in summer (<2000 μmol kg⁻¹ in July) and higher values (>2150 μmol kg⁻¹) in autumn and winter. The north-south difference of TCO₂ is not observed in fCO₂ (Fig. 3a to d). For example, in winter 2019, fCO₂ is slightly below the atmospheric value

with a mean of 374 ± 8 μatm from 10°N to 18°N and a mean of 379 ± 7 μatm from 26°N to 36°N. Normalizing fCO₂ to a constant temperature (NfCO₂) leads to a similar latitudinal distribution to TCO₂ with lower values in the southern region than in the northern one (Fig. 4).

South of 20°N, SST is much higher than north of 20°N, which increases fCO₂ in the southern region. As a result, the temperature impact on fCO₂ is masking the north-south difference of carbon content. The

Table 1
VOS voyages from 10°N to 36°N with dates, name of the ship, latitudinal range and representative month for the year 2019.

| ID	Dates of the voyages	ship	Min lat	Max lat	Representative month
1	3–8 January 2019	*Maersk Raleigh*	10°N	33°N	January
2	5–10 February 2019	*Cap San Lorenzo*	10°N	35°N	February
3	8–11 April 2019	*Cap San Lorenzo*	10°N	35°N	April
4	8–12 May 2019	*Cap San Lorenzo*	10°N	36°N	May
5	28 May-2 June 2019	*Cap San Lorenzo*	10°N	35°N	May
6	2–6 July 2019	*Cap San Lorenzo*	10°N	36°N	July
7	24–28 July 2019	*Cap San Lorenzo*	10°N	31°N	July
8	26–31 August 2019	*Cap San Lorenzo*	10°N	36°N	August
9	17–22 September 2019	*Cap San Lorenzo*	10°N	36°N	September
10	21–25 October 2019	*Cap San Lorenzo*	10°N	35°N	October
11	13–17 November 2019	*Cap San Lorenzo*	10°N	30°N	November
12	16–19 December 2019	*Cap San Lorenzo*	22°N	36°N	December
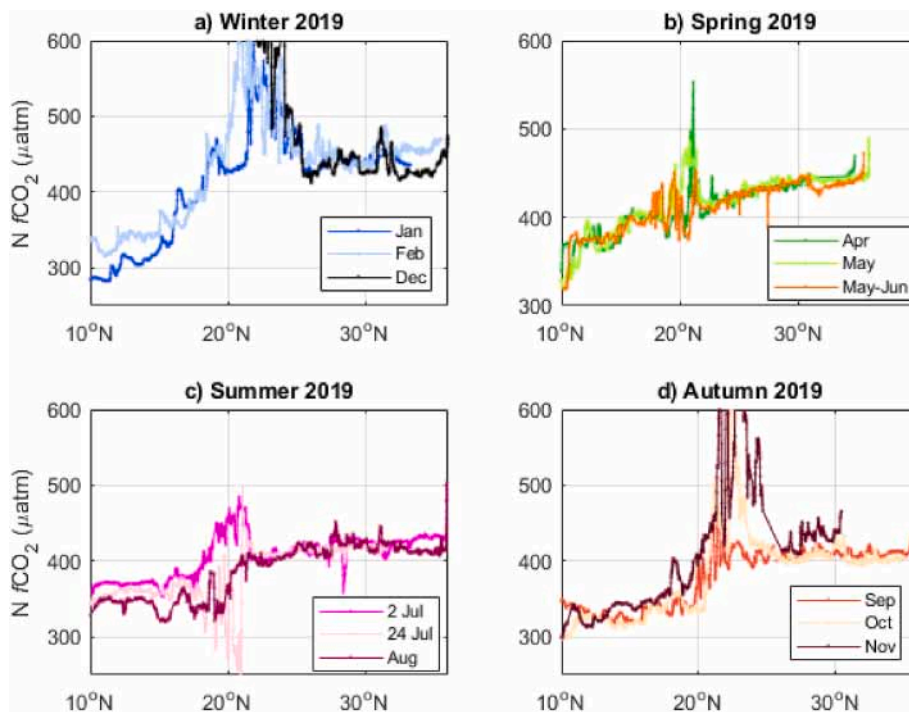
Fig. 4. Normalized fCO$_2$ at a constant temperature of 22 °C in winter, spring, summer and autumn 2019.

supply of carbon is particularly visible in autumn and winter from 20 to 26°N on both the TCO$_2$ and fCO$_2$ distributions (Fig. 3a, d, 3m, 3p). The large CO$_2$ decrease occurring in July 2019 is also observed in both variables (Fig. 3c, o).

Fig. 5 shows the monthly chlorophyll concentrations of 2019 collocated along the track of the *Cap San Lorenzo*, from 10°N to 36°N.

The highest chlorophyll concentrations are located in the permanent upwelling (PU) zone and occur throughout the year. The highest concentrations (>3.7 mg m^{-3}) occur at 20°23′N in summer 2019 and

decrease rapidly with latitude to become lower than 0.2 mg m^{-3} near 22°N. During this season, the peak of high concentrations (>2 mg m^{-3}) is shifted southward compared to months closer to winter season and extends from 18°N to 21°N whereas, at other seasons, the high concentrations tend to spread between 20°N-24°N. The mean seasonal concentrations, along the track from 20°N to 26°N, are always above 0.62 mg m^{-3}. In winter 2019, the mean chlorophyll averages 1.10 ± 0.44 mg m^{-3} in this region (N = 963). The lowest concentrations occur in the northern part of the transect (26°N-36°N). South of 18°N, the
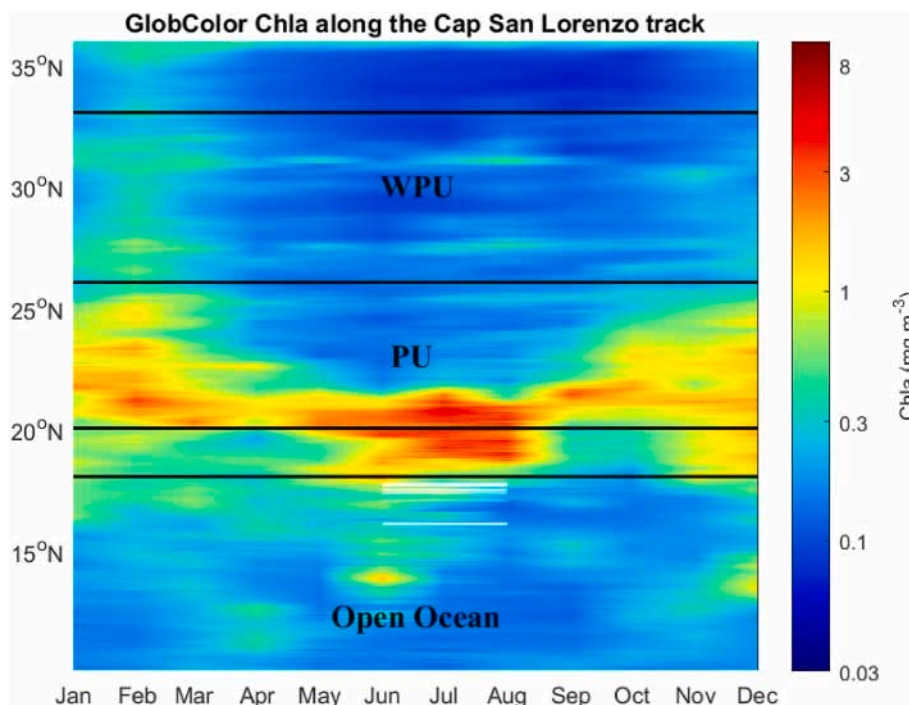

Fig. 5. Monthly chlorophyll concentrations in 2019, along the track of the Cap San Lorenzo from 10°N to 36°N.
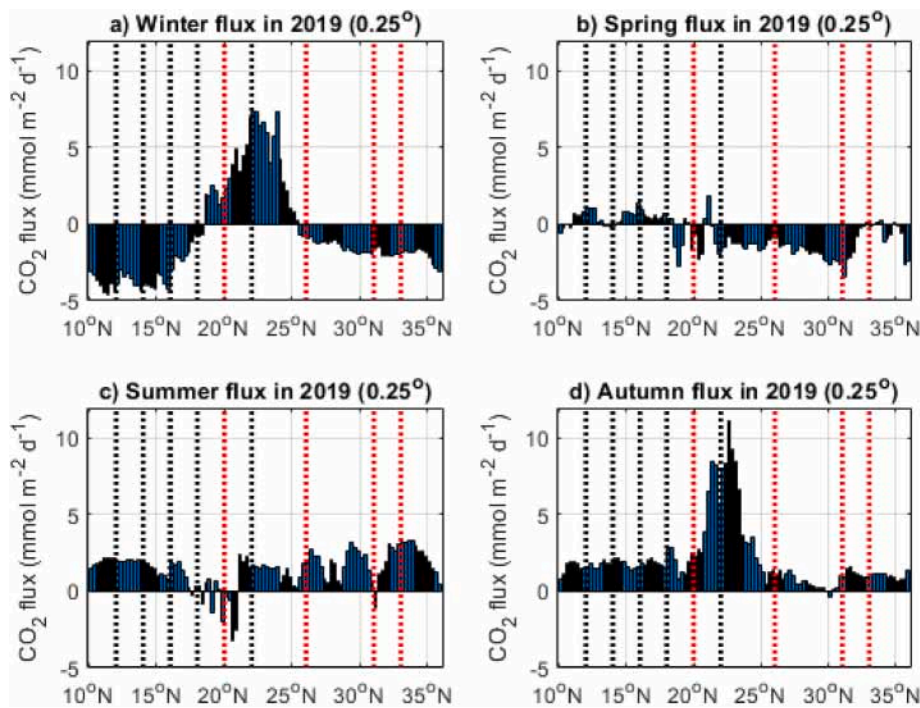
Fig. 6. Bar plots of the CO_2 flux in a) winter (DJF), b) spring (MAM), c) summer (JJA) and d) autumn (SON) 2019 from 10°N to 36°N in 0.25° latitudinal bins. The vertical dashed lines indicate the different regions crossed by the ship. The regions in black are defined by Menna et al. (2016) and correspond to 12-14°N: South Cape Verde (SCV), 14-16°N: Cape Verde (CV), 16-18°N: MA, 18-20°N: Cape Timiris (CT), 20-22°N: Cape Blanc (CB). The regions in red are defined by Siemer et al. (2021) and are the Permanent Upwelling (PU), the Cape Juby Weak Permanent Upwelling (CJWPU), and the Cape Juby Weak Permanent Upwelling (CGWPU).

chlorophyll concentrations are relatively low with seasonal values, averaged between 10°N and 18°N, ranging from 0.20 to 0.29 mg m^{-3}, but they are slightly higher than the chlorophyll concentrations averaged between 26°N and 36°N where mean concentrations range from 0.14 in summer to 0.28 mg m^{-3} in winter 2019. The comparison of the annual concentrations of chlorophyll between 10°N-18°N and 26°N-36°N are significantly different (non-parametric one-tailed test, p-value< 0.0001) with chlorophyll concentrations ranging from 0.17 to 0.47 mg m^{-3} and averaging 0.25 ± 0.06 mg m^{-3} in the south, whereas in the north, they vary between 0.12 and 0.35 mg m^{-3} with a mean of 0.19 ± 0.05 mg m^{-3}. On seasonal time scales, chlorophyll concentrations are similar between the two regions in autumn only.

3.2. Sources and sinks of CO_2 in 2019

Each voyage of 2019 is binned into 0.25° of latitude and grouped by season to determine the sources and sinks of CO_2 along the track of the *Cap San Lorenzo* at each season (Fig. 6).

In winter, the regions 10°N-12°N, the SCV, CV, MA are sinks of CO_2, in contrast to the CT, CB and the PU zone that are sources of CO_2. Further north, the CJWPU, CGWPU and 33°N-36°N are sinks of CO_2 like the southern region. Overall, during this season, three distinct patterns of the CO_2 flux emerge with a sink of CO_2 from 10°N to 18°N, a source of CO_2 from 18°N to 25°N and a sink of CO_2 from 25°N to 36°N (Fig. 6a). These three zones correspond roughly to the main regions identified by Cropper et al. (2014). The regions proposed by Menna et al. (2016) can be grouped together as some regions show the same seasonal source and sink patterns. From 10°N to 16°N, a source of CO_2 occurs in spring (Fig. 6b), summer (Fig. 6c) and autumn (Fig. 6d) whereas the region is a

sink of CO_2 in winter. The southern region from 10°N to 16°N includes the SCV, the CV and the MA regions. Between 18°-20°N, the CT region has similar features to the permanent upwelling zone in winter, spring and autumn. In summer, CT is a sink of CO_2 whereas the southern and permanent upwelling regions are sources of CO_2 (Fig. 6c). This sink of CO_2 coincides with the high chlorophyll concentrations shifted south of 20°N in this season (Fig. 5). The permanent upwelling zone is a source of CO_2 (Fig. 6a, c, 6d) except in spring when it becomes a sink of CO_2 (Fig. 6b, Table 2). The weak upwelling zones of Cape Juby (CJWPU) and Cape Ghir (CGWPU) can be grouped with the area north of 33°N. These three regions are sinks of CO_2 in winter and spring (Fig. 6a and b), and sources of CO_2 in summer and autumn (Fig. 6c and d). The highest CO_2 fluxes occur in winter and autumn (Fig. 6a and d) in the PU with values over 4 mmol m^{-2} d^{-1} (Table 2).

3.3. Drivers of the seasonal variability of fCO₂ in the main regions

The CO_2 source and sink patterns along the track of the *Cap San Lorenzo* highlight three main regions, with a transition zone at Cape Timiris (18°-20°N), that correspond roughly to the latitudinal separation made by Cropper et al. (2014) and Lathuilière et al. (2008). Each voyage of 2019 is averaged on a daily basis in the CGWPU, CJWPU, PU and 10°N-18°N regions to determine the seasonal cycle using equation (7). The coefficients of the equation are given in Table S1 for each parameter. As the seasonal cycles in CGWPU and CJWPU are similar (p < 0.0001), CGWPU and CJWPU are merged into a Weak Permanent Upwelling (WPU) region extending from 26°N to 33°N. In this region, fCO_2 ranges from 375 µatm in winter to 415 µatm in summer (Fig. 7a).

In the WPU, the fCO_2 follows the same variations as SST (Fig. 7b). The salinity averages 36.48 ± 0.10 and its amplitude is less than 0.3. The upwelling is expected to lower the surface salinity as subsurface waters are fresher (Vélez-Belchí et al., 2017). The monthly fCO_2 observations are strongly correlated with SST (r^2 = 0.90 and RMSE = 4.5 µatm) in WPU. The salinity does not improve the correlation, which suggests that SST controls most of the CO_2 variations. The relationship between fCO_2 and SST corresponds to an increase of fCO_2 of about 2.2%/°C, which is lower than the thermodynamical increase of 4%/°C if warming is the only process affecting the CO_2 variations (Fig. 8).
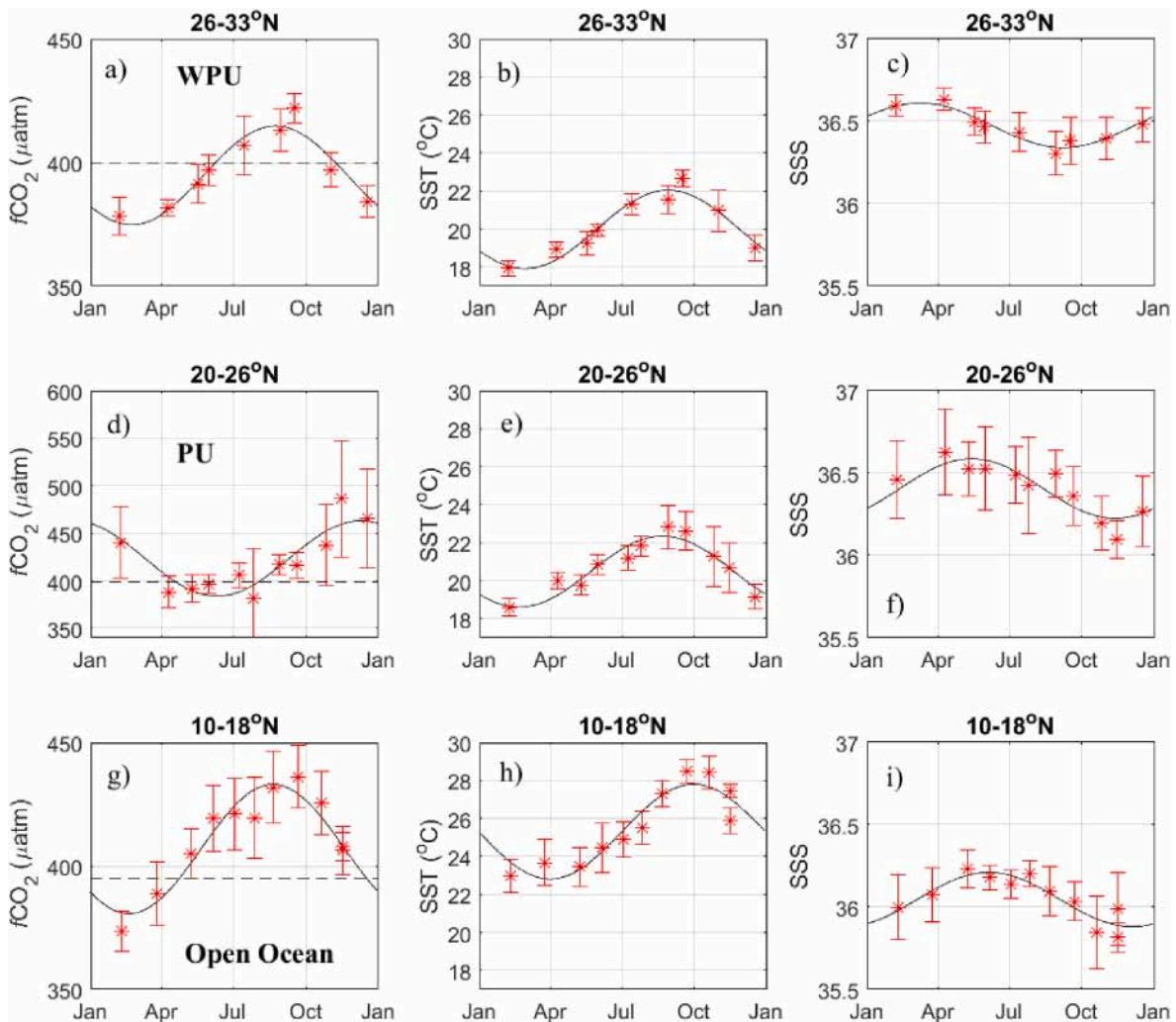
Table 2
Seasonal CO_2 flux (mean and standard deviation, in mmol m^{-2} d^{-1}) along the track of the *Cap San Lorenzo* in 2019.

Region	Winter (DJF)	Spring (MAM)	Summer (JJA)	Autumn (SON)
10°N-18°N	−2.60 ± 0.78	0.41 ± 0.46	1.59 ± 0.63	1.73 ± 0.29
20°N-26°N	4.31 ± 2.95	−1.34 ± 0.95	0.90 ± 1.39	4.76 ± 3.14
26°N-33°N	−1.86 ± 0.37	−1.95 ± 0.93	1.85 ± 1.01	0.75 ± 0.51

Fig. 7. Seasonal cycle of fCO$_2$, SST and SSS for the WPU (26-33°N), PU (20-26°N) and open ocean (10-18°N) in 2019. Note the different scale in panel d) for fCO$_2$. The black curve corresponds to the seasonal cycle represented by the harmonic fit. The means and standard deviations of the observations are in red.
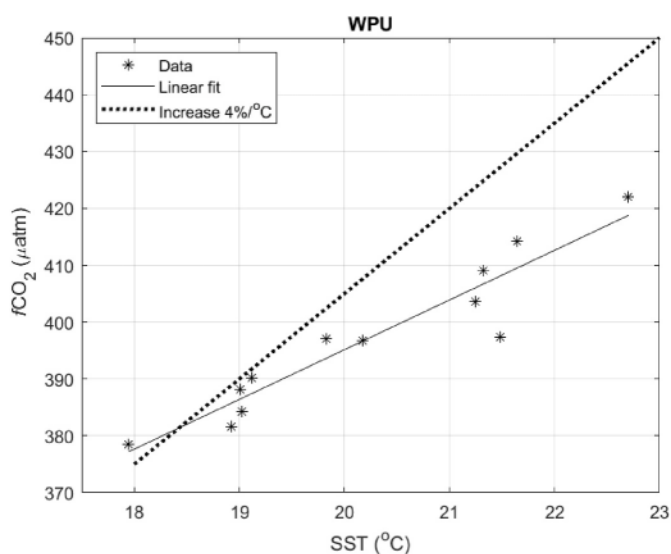

Fig. 8. Observations of fCO$_2$ as a function of SST in 2019 in the WPU region. The black line corresponds to the linear fit between fCO$_2$ and SST. The increase of fCO$_2$ with SST is lower than the thermodynamic increase of 4%/°C (dashed line).

In the PU zone, the fCO$_2$ variations do not follow the seasonal cycle of SST. As very high fCO$_2$ values are encountered in this region, the scale of Fig. 7d is different from the other regions. The lowest fCO$_2$ occur in June and the highest fCO$_2$ are in autumn-winter (Fig. 7d) whereas the SST peaks in August (Fig. 7e) and is minimum in February. The lowest fCO$_2$ are observed at the period of highest chlorophyll concentrations (Fig. 5). The variability of fCO$_2$ in PU is twice as large as the one in WPU but the amplitude of SST is similar and less than 4 °C. The salinity averages 36.42 ± 0.12 with an amplitude less than 0.4. The largest CO$_2$ source in PU (black line in Fig. 7d) is associated with the lowest SST and reveal the signature of the upwelling although the correlation is low (−0.22, p-value <0.0001). The correlation between the seasonal cycles of fCO$_2$ and SSS is significantly higher with a coefficient of −0.86. The relationship between observations of fCO$_2$ and both SST and SSS gives a determination coefficient r^2 of 0.79 and a RMSE of 15 µatm.

In the open ocean section of the transect, fCO$_2$ averages 404 ± 22 µatm, and presents a maximum in August and a minimum in February (Fig. 7g) as in the WPU (Fig. 7a). The SST seasonal cycle is shifted by a month, compared to fCO$_2$ and to SST in the other regions, with a minimum in March and a maximum in September (Fig. 7h). This region is much warmer with a mean SST of 25.32 ± 1.82 °C and the salinity is lower with a mean of 36.05 ± 0.11. Observations of fCO$_2$ are correlated with SST (r = 0.66) but SST explains only 44% (r^2 = 0.44) of the fCO$_2$ variations. The fCO$_2$ data can be expressed as a function of SST and SSS (r^2 = 0.85, RMSE = 10 µatm).
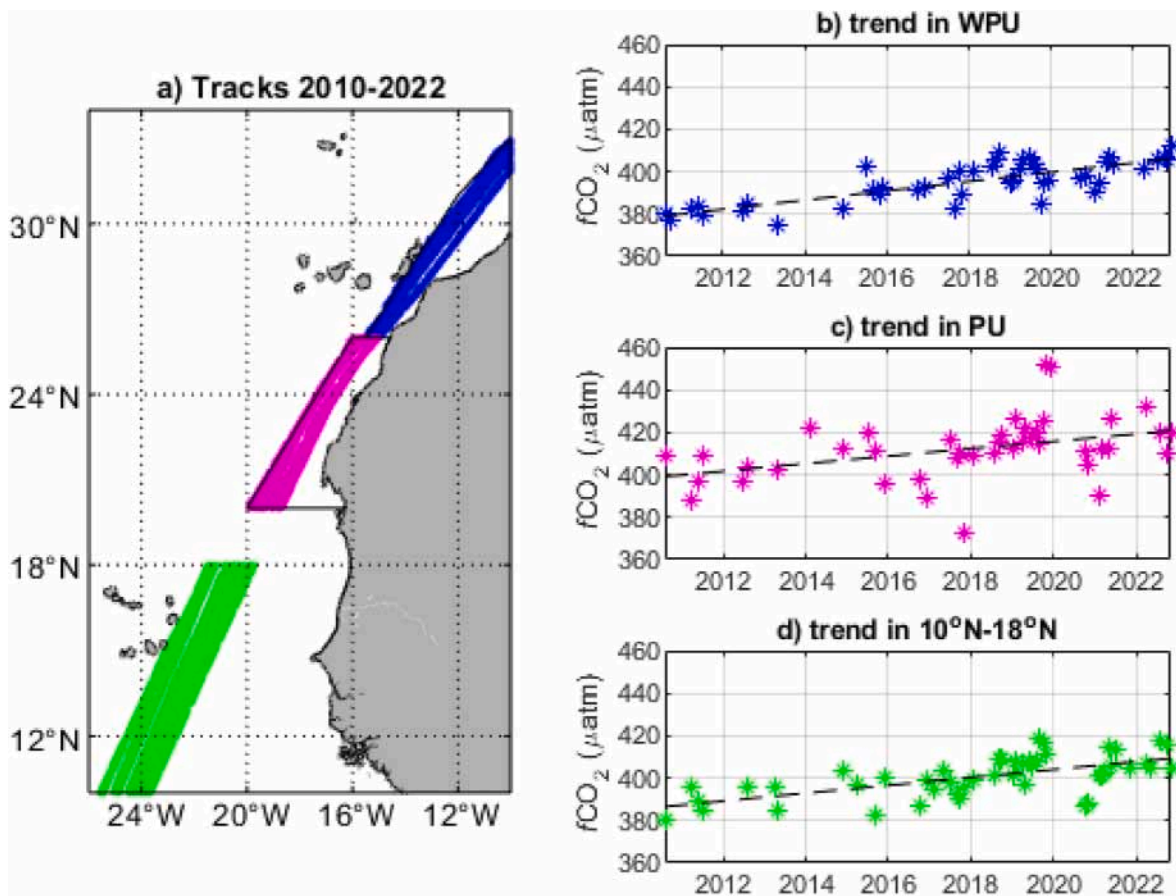
Fig. 9. a) Tracks of the ship in each region where the trend of fCO_2 is calculated. Monthly fCO_2 anomalies added to the mean value of fCO_2 in the b) WPU region, c) the PU region and d) the 10°N-18°N region from August 2010 to August 2022. The dashed line is the trend (in µatm yr^{-1}) calculated in each region.

The calculation of the relative importance of thermal processes over non-thermal processes on fCO_2 indicates that the thermodynamical processes dominate in the WPU and in the southern part of the transect with the ratio of thermodynamic over other processes, T/B values, of 2.11 and 1.39 respectively. On the contrary, in the PU, biological and mixing processes are dominant with T/B lower than 1 with a value of 0.61.

Using the data binned by 0.25° of latitude, we examine the spatial correlations between fCO_2, SST, SSS, TCO$_2$ and the chlorophyll concentrations in 2019 within each season. For example, all the data of the transects realized in winter 2019 (December, January and February 2019) are gathered to examine the correlations between the pairs of parameters in each region. In the WPU, fCO_2 and TCO$_2$ are negatively correlated with chlorophyll in spring (r = −0.38, p < 0.05) and summer (r = −0.83, p < 0.0001 for fCO_2 and r = −0.57, p < 0.005 for TCO$_2$) but chlorophyll concentrations are lower than 0.3 mg m^{-3} in this part of the transect. In the PU, high chlorophyll concentrations occur throughout the year (Fig. 5). Values of fCO_2 are also high, especially in autumn and winter (Fig. 7d) leading to strong outgassing (Fig. 6a and d), which is characteristic of colder and CO$_2$-rich upwelled waters. The correlation fCO_2-chlorophyll is positive in winter, with a value of 0.81 (p < 0.0001). A negative correlation occurs in summer only with a coefficient of −0.67 (p < 0.0005). However, a stronger correlation is observed with TCO$_2$ and chlorophyll in summer and spring with coefficients of −0.90 (p < 0.0001) and −0.89 (p < 0.0001) respectively. As for fCO_2, the correlation of TCO$_2$ with chlorophyll is positive in winter (r = 0.72, p = 0.0001) but the TCO$_2$-chlorophyll correlation is not significant in autumn (r = 0.06, p = 0.78). The biological impact on the inorganic carbon parameters are examined at a higher spatial resolution (Figs. S1–S6) and confirm the results obtained here. In July, the ship sampled the region

twice and a strong decrease of fCO_2 is observed when the high chlorophyll concentrations extend offshore (Figs. S1, S5, S6). In the southern region, 10°N-18°N, there is no significant correlation between fCO_2 and chlorophyll. TCO$_2$ is positively correlated with chlorophyll in winter (0.68, p < 0.0001) and spring (0.70, p < 0.0001) but chlorophyll concentrations are, on average, lower than 0.30 mg m^{-3}.

3.4. Temporal trends of fCO_2 in the upwelling regions and in the open ocean section

In this section, we evaluate whether a long-term trend can be inferred from the analysis of the selected voyages in the WPU, PU and in the open ocean section (Fig. 9a). The longitudinal variability between the voyages in each region is less than 2°. The trends are calculated from the monthly anomalies of fCO_2 over the 2010–2022 period. In each region, the seawater fCO_2 increases significantly over time (Fig. 9b-d). In

Table 3
Trends of fCO_2, SST, SSS, TCO$_2$ and pH in the WPU, PU and 10°N-18°N regions calculated using the ship observations from 2010 to 2022.

Trends	WPU	PU	10°N-18°N
fCO_2 (µatm yr^{-1})	2.10 ± 0.26	1.82 ± 0.64	1.91 ± 0.34
SST (°C yr^{-1})	−0.04 ± 0.02[a]	−0.13 ± 0.04	−0.04 ± 0.03[a]
SSS (yr^{-1})	−0.019 ± 005	−0.017 ± 007	−0.002 ± 007[a]
TCO$_2$ (µmol.kg^{-1} yr^{-1})	0.70 ± 0.23	1.14 ± 0.51	1.24 ± 0.53
pH (yr^{-1})	−0.0020 ± 0.0002	−0.0016 ± 0.0005	−0.0016 ± 0.0003
Chla (mg m^{-3} yr^{-1})	0.006 ± 0.002	0.008 ± 0.009[a]	0.008 ± 0.002

[a] The trend is not significant at the 5% level.

the same way, the trends are calculated for SST, SSS, TCO$_2$, and pH (Table 3). The trend of the chlorophyll concentrations are calculated over the same period, 2010–2022, using the satellite data.

The increase of fCO$_2$ is not significantly different from one region to another. As expected, the increase of fCO$_2$ corresponds to a significant decrease of pH in each oceanic region and to an increase of TCO$_2$. In the WPU, the SST decrease is not significant at the 5% level. In the open ocean region, there is no trend in SST and SSS. In the regions with very low chlorophyll concentrations, WPU and 10°N-18°N, chlorophyll increases slightly over time. In the PU region, no significant trend of chlorophyll is detected.

The rates of increase of seawater fCO$_2$ in each region are not statistically different from the atmospheric increase of 2.53 ± 0.07 µatm yr^{-1} over the 2010–2022 period (p-value >0.07).

With the oceanic and atmospheric fCO$_2$ increasing at about the same rate in each region, the difference of fCO$_2$ between the ocean and the atmosphere does not present any trend. In addition, no significant trend is detected in the CO$_2$ flux over 2010–2022.

4. Discussion

4.1. Impact of the upwelling on the CO$_2$ flux variability and its drivers

The underway SST and SSS measured during the voyages of the *Cap San Lorenzo* and the *Maersk Raleigh* are in good agreement with the satellite SST and SSS averaged monthly in the weak and permanent upwelling regions. Therefore, the observations collected by the ships are assumed representative of the processes occurring in these two upwelling regions.

In the WPU, the seasonal variability of fCO$_2$ is mainly driven by SST patterns with maximum values in summer. The thermal effect is confirmed by a value of the T/B ratio higher than 2. These results are in good agreement with the work of Curbelo-Hernández et al. (2021) who estimated the seasonal CO$_2$ flux using data from a volunteer observing ship from February 2019 to February 2020 between the Strait of Gibraltar (36°N) and the Canary Islands (28°N). Although their VOS line

sails a bit further offshore than the *Cap San Lorenzo*, slightly outside the WPU area, the fCO$_2$ values measured between 28°N and 36°N are similar (Table S2). They also report SST as the main driver of seasonal fCO$_2$ variations with an increase of fCO$_2$ with SST lower than the thermodynamical relationship of 4%/°C, as observed in the WPU. In the WPU, the chlorophyll concentrations are low and fCO$_2$ values remain close to open ocean values. Satellite images of chlorophyll show that high concentrations (up to 9 mg m^{-3}) are confined to the shelf as previously reported (Lathuilière et al., 2008). In 2019, the monthly chlorophyll concentration in the whole WPU area is below 0.63 mg m^{-3}. In this region, the origin of the upwelling water is the NACW that is relatively poor in nutrients, whereas, south of Cape Blanc, the origin of the seasonal coastal upwelling is the SACW, much richer in nutrients (Demarcq and Somoue, 2015). The Cape Verde frontal zone separates the northern subtropical water from the water of tropical origin in the south (Kämpf and Chapman, 2016a). Between 10°N and 18°N, chlorophyll concentrations are relatively higher than from 26°N to 36°N along the track of the ship. However, the chlorophyll concentrations remain low as the ship sails further offshore the productive region. TCO$_2$ is also significantly lower than in the upwelling regions (Fig. 3), especially south of the Cape Verde Arquipelago (~15°N). The warm waters with low chlorophyll and TCO$_2$ concentrations could be explained by advection of surface waters from the NECC. The NECC is a zonal current flowing eastward across the tropical Atlantic from the coast of South America to the coast of Africa. During its journey, it is affected by high precipitation associated with the Intertropical Convergence Zone (ITCZ). A north-south gradient of TCO$_2$ has been reported between the NECC and the westward NEC flowing further north of the NECC. Due to the influence of the ITCZ, the NECC is fresher and lower in carbon content than the NEC (e.g. Bonou et al., 2016). The TCO$_2$ gradient between the upwelling regions and the open ocean region does not appear so strongly on seawater fCO$_2$. The high SST encountered in the tropical region increases fCO$_2$, which reaches similar values as in WPU. In both regions, SST is an important driver of fCO$_2$ variability but the salinity is also an important driver of fCO$_2$ at seasonal scale in the open ocean region. This is probably associated to the different northern and southern water
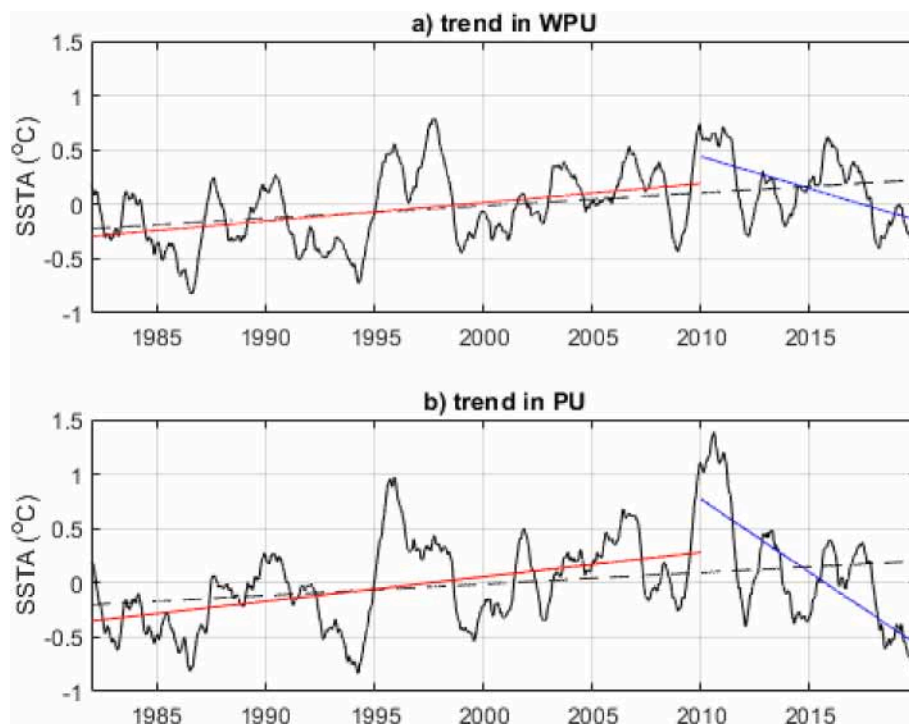

Fig. 10. SST anomalies (SSTA) from 1982 to 2019 in the a) WPU region and b) in the PU region. The dashed line corresponds to the trend over the whole period, the red line from 1982 to 2009 and the blue line from 2010 to 2019.

masses mixing near the Cape Verde Frontal Zone.

Unlike the WPU and the southern region, the PU region has a T/B ratio lower than 1, which excludes thermodynamics as the dominant process here. The spatial extension of the chlorophyll concentrations is maximum in the PU zone (Lathuilière et al., 2008) and the ship samples the highest values between 20°N-26°N as shown by the Hovmöller diagram (Fig. 5). However, the carbon uptake by the phytoplankton is not sufficient to cause a CO_2 drawdown and the fCO_2 values and the CO_2 flux are the highest in the PU. Overall, along the track of the ship, chlorophyll and fCO_2 are correlated in winter (r = 0.92) and autumn 2019 (r = 0.78) as both strong carbon supply and biological activity are occurring. The Mercator-Ocean model simulations at 1/12° resolution (Lellouche et al., 2021) show that the mixed layer depth is deeper in autumn and winter compared to spring and summer in both PU and WPU regions. Despite the high productivity, overall the CO_2 flux in PU is much larger than in the WPU and in the open ocean. Closer to the coast, along 18°N, Steinhoff et al. (2012) measured values reaching 650 μatm because of the upwelling. They observed decreasing values as the ship sailed offshore with near-equilibrium conditions near 17.5°W. In this region, along the track of the *Cap San Lorenzo*, strong local sinks of CO_2 were observed. In July 2019, fCO_2 decreased from 433 ± 12 μatm on the 3rd of July to 294 ± 41 μatm on the 26th of July, below the atmospheric value of 396.2 ± 1.8 μatm for July 2019, between 20°N and 21°N. Similarly, Loucaides et al. (2012), following an upwelling filament moving offshore, reported that phytoplankton depleted seawater carbon dioxide concentrations far below the atmospheric level.

In the PU region, the fCO_2 variability is mainly driven by the upwelling, with highest CO_2 values in autumn and winter. It is a highly productive region and the offshore chlorophyll extension affects the CO_2 distribution. The fCO_2 variability in the WPU is mainly driven by temperature variations as chlorophyll concentrations remain low. In the open ocean part of the transect, temperature and salinity are governing the CO_2 variations.

4.2. Trends in CO_2 and upwelling over the 2010–2022 period

The evolution of the CO_2 flux in the WPU and PU regions will be likely affected by physical processes, such as the intensification or reduction of the coastal upwelling, and changes in productivity.

In the PU region, we observe a significant decrease of SST -0.13 °C yr^{-1} from 2010 to 2022 (Table 3). An intensification of the upwelling would lead to a cooling of coastal waters, which would be detected by a decreasing SST trend, and more CO_2-rich water coming up to the surface layer. This is what is observed by González-Dávila et al. (2017) who found a negative SST trend of −0.2 °C yr^{-1} at Cape Blanc (21°N) and Cape Verde (15°N) over 2005–2012 using observations from their QUIMA VOS line. This upwelling intensification was associated to an increase of seawater fCO_2 of 2.5 ± 0.4 μatm yr^{-1}, which is higher than the increase of atmospheric fCO_2. This corresponds to a decrease of pH of 0.003 ± 0.001 yr^{-1}.

The monthly SST fields from MODIS, at 4 km resolution, confirm the decrease of SST in the upwelling regions over 2010–2022. SST decreases significantly at a rate of −0.03 ± 0.01 °C yr^{-1} in WPU and −0.07 ± 0.02 °C yr^{-1} in PU. These results are consistent with the trends calculated from the ship observations (Table 3). The decrease in the 10°N-18°N band is not significant. Over a much longer period (1982–2019), Siemer et al. (2021) found a warming trend in the WPU and PU regions. They found significant increasing SST trends, ranging from 0.0023 to 0.0114 °C yr^{-1}, in the CGWPU, CJWPU, PU regions (cf their Table 1) over the 1982–2019 and 1992–2019 periods, associated with a decrease in chlorophyll concentrations, from 1998 to 2018, and in net primary production from 2003 to 2018. This warming trend is consistent with the results of Barton et al. (2013) who detected SST increase at a rate of 0.01 °C yr^{-1} from 1967 to 2007 and twice this rate for the shorter period 1985–2007. In both studies, the rate of SST increase differs according to the length of the time series. Using the same SST fields over the

1982–2019 period, there is evidence of a decrease of SST in WPU and PU over the 2010–2019 period, consistent with our observations (Fig. 10). In 2010, the North Atlantic Ocean experienced an anomalous surface warming leading to an increase of seawater fCO_2 (e.g. Ibánhez et al., 2017). The anomalous warming is clearly visible on the series of SST anomalies with a positive SSTA higher than 0.5 °C in WPU and over 1 °C in PU (Fig. 10). With a start date of the trend characterized by a strong positive anomaly, the SST trend calculated from 2010 is decreasing with a slope reaching −0.135 ± 0.002 °C yr^{-1} in the PU region over the 2010–2019 period.

Further offshore the WPU region, monthly fCO_2 has been monitored at the ESTOC station located at 29°10' N, 15°30' W. The seawater fCO_2 at ESTOC has increased at a rate of 1.9 ± 0.3 μatm yr^{-1} and pH has decreased at a rate of 0.0019 ± 0.0003 yr^{-1} from 1995 to 2014 (Santana-Casiano and González-Dávila, 2015), which is not significantly different from the fCO_2 and pH trends observed in the WPU (Table 3). This is in agreement with the results of Roobaert et al. (2019) who found similar patterns with the coastal region and adjacent open ocean.

In the PU region, despite SST and wind trends suggesting an upwelling intensification, the rate of seawater fCO_2 increase is similar to the atmospheric CO_2 increase. Overall, there is no consensus as whether the intensity of the CCUS is increasing (Abrahams et al., 2021; Benazzouz et al., 2015). Varela et al. (2015) pointed out that the study area, the season, the length of the time series and even the database used might explain the diversity of trends, hence the contradictory results.

The variability associated with climate modes could also explain the different trends observed at various time scales. The CCUS is mainly affected by the North Atlantic Oscillation (NAO) and the East Atlantic (EA) patterns (Georg et al., 2022). The NAO index indicates the differences in atmospheric pressure patterns in the North Atlantic, characterized by low pressure over Icelandic and high pressure over the Azores (Hurrell, 1995). During the positive NAO phase, the westerly winds intensify, strengthening the upwelling and deepening the mixed layer along the coast. In its negative phase, this is the opposite. The EA pattern consists of a north-south dipole of anomalies, shifted southeastward relative to NAO. According to Georg et al. (2022), both NAO phases are intensified in years with a coupled opposite phase of the EA pattern, mainly in winter, when both indices effects are intensified.

Analyzing the signals of NAO and EA indices with a 12-month low-pass filter, we identified a positive trend of 0.04 yr^{-1} in the NAO index and 0.21 yr^{-1} in the EA index for the period from January 2010 to September 2022. However, NAO has been trending in a negative phase since 2019. During 2019, the NAO index was in its negative phase (~−1), and EA was in its positive phase (~+1). Following the potential temperature composite analyses performed by Georg et al. (2022) for opposite NAO and EA phases, in the case of a combination of NAO+ with EA-, it suggests a weakening of the upwelling spatial extension in the CCUS region during 2019. Using numerical simulations, Brady et al. (2019) conclude that the CCUS has anomalous outgassing during a positive phase of the NAO. On a longer time scale, 1993–2014, Gómez-Letona et al. (2017) show a stronger impact of the NAO on seasonal SST in the PU zone in winter and autumn.

The trends found here are calculated on a short period, from 2010 to 2022, when CO_2 observations are available. A negative trend of SST is detected in the PU region only over this time period whereas Siemer et al. (2021), for example, found warming trends in WPU and PU and a decrease of chlorophyll concentrations. The study of pCO_2 trends of Fay and McKinley (2013) shows that the trend depends on the time period as well as the start date and the end date of the time series. According to Barton et al. (2013), for SST or wind series shorter than 30 years, the trends vary widely and might even change sign. This explains the negative trend of SST observed over 2010–2022, and by González-Dávila et al. (2017) over 2005–2012, whereas Siemer et al. (2021) report a warming trend in WPU and PU.

Although we observe a negative SST trend in the PU zone, the upwelling intensification is not strong enough to lead to a noticeable

increase of CO_2 outgassing and seawater fCO_2 increases at a similar rate as the atmospheric fCO_2 over 2010–2022. A longer time series of seawater fCO_2 in the CCUS is required to detect robust trends and to better understand the sensitivity of the CO_2 fluxes to the different modes of climate variability.

Although voluntary observing ships are sampling surface waters only, they are very useful for dynamical systems, such as coastal upwellings, because of their repeat voyages. Observations at seasonal scales would be difficult to achieve with oceanographic cruises only. A growing dataset will enable us to get better insights in the variability and trends of fCO_2 in these complex systems.

5. Conclusions

In 2019, the voyages of two merchant ships sailing close to the African coast, on the same tracks, between 10°N and 36°N, highlighted three main regions with different seasonal patterns of the air-sea flux of CO_2. The open ocean transect (10-18°N) is a sink of CO_2 of -2.60 ± 0.78 mmol m^{-2}d^{-1} in winter (DJF) only. The permanent upwelling region (20-26°N) is always a source of CO_2 except in spring when biological consumption dominates, which causes a sink of CO_2 of -1.34 ± 0.95 mmol m^{-2}d^{-1}. The strongest sources of CO_2 occur in this region in autumn (4.76 ± 3.14 mmol m^{-2}d^{-1}) and winter (4.31 ± 2.95 mmol m^{-2}d^{-1}). This region is dominated by upwelling dynamics including supply of carbon and biological CO_2 drawdown. High chlorophyll concentrations occur throughout the year, and spread offshore, making it the most productive region.

The weak permanent upwelling region (26-33°N) is a sink of CO_2 in winter and spring (MAM) and a source of CO_2 in summer (JJA) and autumn (SON) with CO_2 fluxes ranging from -1.95 ± 0.93 mmol m^{-2}d^{-1} in spring to 1.85 ± 1.01 mmol m^{-2}d^{-1} in summer. High productivity and strong cooling are restricted to the continental shelf. At seasonal scale, the CO_2 variability is mainly controlled by thermodynamical processes. Although strong CO_2 outgassing is observed in the PU zone in 2019, the coastal upwelling is probably weak because the NAO is in negative phase in 2019.

From 2010 to 2022, seawater fCO_2 increases significantly in each region but the rate of fCO_2 increase does not present statistical difference from the rate of increase of atmospheric CO_2 and the CO_2 flux does not exhibit any significant trend. Longer time series (>30 years) are required to detect robust trends, which highlights the importance of programs of long term monitoring of fCO_2.

Declaration of competing interest

The authors declare that they have no known competing financial interests or personal relationships that could have appeared to influence the work reported in this paper.

Data availability

The data are publicly available

Appendix A. Supplementary data

Supplementary data to this article can be found online at https://doi.org/10.1016/j.dsr.2023.104130.

References

Abrahams, A., Schlegel, R.W., Smit, A.J., 2021. Variation and change of upwelling dynamics detected in the world's eastern boundary upwelling systems. Front. Mar. Sci. 8.

Arístegui, J., Barton, E.D., Álvarez-Salgado, X.A., Santos, A.M.P., Figueiras, F.G., Kifani, S., Hernández-León, S., Mason, E., Machú, E., Demarcq, H., 2009. Sub-regional ecosystem variability in the Canary Current upwelling. Prog. Oceanogr. 83 (1), 33–48.

Barton, E.D., Field, D.B., Roy, C., 2013. Canary current upwelling: more or less? Prog. Oceanogr. 116, 167–178.

Benazzouz, A., Demarcq, H., González-Nuevo, G., 2015. Recent Changes and Trends of the Upwelling Intensity in the Canary Current Large Marine Ecosystem. Trends of the Upwelling Intensity in the CCLME. IOC-UNESCO.

Bonino, G., Di Lorenzo, E., Masina, S., Iovino, D., 2019. Interannual to decadal variability within and across the major eastern boundary upwelling systems. Sci. Rep. 9 (1), 19949.

Bonino, G., Lovecchio, E., Gruber, N., Münnich, M., Masina, S., Iovino, D., 2021. Drivers and impact of the seasonal variability of the organic carbon offshore transport in the Canary upwelling system. Biogeosciences 18 (8), 2429–2448.

Bonou, F.K., Noriega, C., Lefèvre, N., Araujo, M., 2016. Distribution of CO_2 parameters in the western tropical Atlantic Ocean. Dynam. Atmos. Oceans 73, 47–60.

Borges, A.V., Frankignoulle, M., 2002. Distribution of surface carbon dioxide and air-sea exchange in the upwelling system off the Galician coast. Global Biogeochem. Cycles 16 (2), 13-11-13-13.

Brady, R.X., Lovenduski, N.S., Alexander, M.A., Jacox, M., Gruber, N., 2019. On the role of climate modes in modulating the air–sea CO2 fluxes in eastern boundary upwelling systems. Biogeosciences 16 (2), 329–346.

Carr, M.-E., 2001. Estimation of potential productivity in Eastern Boundary Currents using remote sensing. Deep Sea Res. Part II Top. Stud. Oceanogr. 49 (1), 59–80.

Cropper, T.E., Hanna, E., Bigg, G.R., 2014. Spatial and temporal seasonal trends in coastal upwelling off Northwest Africa, 1981–2012. Deep Sea Res. Oceanogr. Res. Pap. 86, 94–111.

Curbelo-Hernández, D., González-Dávila, M., González, A.G., González-Santana, D., Santana-Casiano, J.M., 2021. CO2 fluxes in the Northeast Atlantic Ocean based on measurements from a surface ocean observation platform. Sci. Total Environ. 775, 145804.

Demarcq, H., Somoue, L., 2015. Phytoplankton and Primary Productivity off Northwest Africa. Phytoplanktonic Productivity off NW Africa. IOC-UNESCO.

Dickson, A.G., Millero, F.J., 1987. A comparison of the equilibrium constants for the dissociation of carbonic acid in seawater media. Deep Sea Res. 34, 1733–1743.

Diogoul, N., Brehmer, P., Demarcq, H., El Ayoubi, S., Thiam, A., Sarre, A., Mouget, A., Perrot, Y., 2021. On the robustness of an eastern boundary upwelling ecosystem exposed to multiple stressors. Sci. Rep. 11 (1), 1908.

Edmond, J.M., 1970. High precision determination of titration alkalinity and total carbon dioxide content of seawater by potentiometric titration. Deep Sea Res. 17 (4), 737–750.

Failler, P., 2020. Fisheries of the canary current large marine ecosystem: from capture to trade with a consideration of migratory fisheries. Environmental Development 36, 100573.

Fay, A.R., McKinley, G.A., 2013. Global trends in surface ocean pCO2 from in situ data. Global Biogeochem. Cycles 27 (2), 541–557.

Georg, T., Neves, M.C., Relvas, P., 2022. The signature of NAO and EA climate patterns on the vertical structure of the Canary Current Upwelling System. EGUsphere 2022, 1–14.

Gómez-Letona, M., Ramos, A.G., Coca, J., Arístegui, J., 2017. Trends in primary production in the canary current upwelling system—a regional perspective comparing remote sensing models. Front. Mar. Sci. 4.

González-Dávila, M., Santana Casiano, J.M., Machín, F., 2017. Changes in the partial pressure of carbon dioxide in the Mauritanian–Cap Vert upwelling region between 2005 and 2012. Biogeosciences 14 (17), 3859–3871.

Gregor, L., Monteiro, P.M.S., 2013. Is the southern Benguela a significant regional sink of CO2? : research letter. South Afr. J. Sci. 109 (5), 1–5.

Hurrell, J.W., 1995. Decadal trends in the North atlantic oscillation: regional temperatures and precipitation. Science 269 (5224), 676–679.

Ibánhez, J.S.P., Flores, M., Lefèvre, N., 2017. Collapse of the tropical and subtropical North Atlantic CO2 sink in boreal spring of 2010. Sci. Rep. 7, 1–9.

Jiang, Z.-P., Hydes, D.J., Hartman, S.E., Hartman, M.C., Campbell, J.M., Johnson, B.D., Schofield, B., Turk, D., Wallace, D., Burt, W.J., Thomas, H., Cosca, C., Feely, R., 2014. Application and assessment of a membrane-based pCO2 sensor under field and laboratory conditions. Limnol Oceanogr. Methods 12 (4), 264–280.

Kämpf, J., Chapman, P., 2016a. The Canary/Iberia Current Upwelling System. Upwelling Systems of the World: A Scientific Journey to the Most Productive Marine Ecosystems. Springer International Publishing, Cham, pp. 203–250.

Kämpf, J., Chapman, P., 2016b. The Functioning of Coastal Upwelling Systems. Upwelling Systems of the World: A Scientific Journey to the Most Productive Marine Ecosystems. Springer International Publishing, Cham, pp. 31–65.

Lathuilière, C., Echevin, V., Lévy, M., 2008. Seasonal and intraseasonal surface chlorophyll-a variability along the northwest African coast. J. Geophys. Res.: Oceans 113 (C5).

Lee, K., Tong, L.T., Millero, F.J., Sabine, C., Dickson, A.G., Goyet, C., Park, G.-H., Wanninkhof, R., Feely, R.A., Key, R.M., 2006. Global relationships of total alkalinity with salinity and temperature in surface waters of the world's oceans. Geophys. Res. Lett. 33, L19605 https://doi.org/10.1029/2006GL027207.

Lefèvre, N., Mejia, C., Khvorostyanov, D., Beaumont, L., Koffi, U., 2021. Ocean circulation drives the variability of the carbon system in the eastern tropical atlantic. Oceans 2 (1), 126–148.

Lellouche, J.-M., Greiner, E., Bourdallé-Badie, R., Garric, G., Melet, A., Drévillon, M., Bricaud, C., Hamon, M., Le Galloudec, O., Regnier, C., 2021. The Copernicus global 1/12 oceanic and sea ice GLORYS12 reanalysis. Front. Earth Sci. 9, 698876.

Liu, M., Tanhua, T., 2021. Water masses in the Atlantic Ocean: characteristics and distributions. Ocean Sci. 17 (2), 463–486.

Llinas, O., Rodriguez de Leon, A., Siedler, G., Wefer, G., 1994. The ESTOC time series station started operation. WOCE Newsletter 17, 20.

Loucaides, S., Tyrrell, T., Achterberg, E.P., Torres, R., Nightingale, P.D., Kitidis, V., Serret, P., Woodward, M., Robinson, C., 2012. Biological and physical forcing of carbonate chemistry in an upwelling filament off northwest Africa: results from a Lagrangian study. Global Biogeochem. Cycles 26 (3).

Mehrbach, C., Culberson, C.H., Hawley, J.E., Pytkowicz, R.M., 1973. Measurement of the apparent dissociation constants of carbonic acid in seawater at atmospheric pressure. Limnol. Oceanogr. 18, 897–907.

Menna, M., Faye, S., Poulain, J.-M., Centurioni, L., Lazar, A., Gaye, A., Sow, B., Dagorne, D., 2016. Upwelling features off the coast of north-western Africa in 2009-2013. Boll. Geofis. Teor. Appl. 57 (1), 71–86.

Mittelstaedt, E., 1983. The upwelling area off Northwest Africa—a description of phenomena related to coastal upwelling. Prog. Oceanogr. 12 (3), 307–331.

Monteiro, P., 2010. Eastern Boundary Currents: the Benguela Current System. Carbon and Nutrient Fluxes in Continental Margins: A Global Synthesis. Springer, New York, pp. 64–77.

Park, G.-H., Wanninkhof, R., 2012. A large increase of the CO2 sink in the western tropical North Atlantic from 2002 to 2009. J. Geophys. Res. 117 (C080029) https://doi.org/10.1029/2011JC007803.

Pastor, M.V., Vélez-Belchí, P., Hernández-Guerra, A., 2015. Water Masses in the Canary Current Large Marine Ecosystem. Water Masses in the CCLME. IOC-UNESCO.

Pelegrí, J.L., Benazzouz, A., 2015. Coastal Upwelling off North-West Africa. Instituto Español de Oceanografía. Intergovernmental Oceanographic Commission.

Pelegrí, J.L., Peña-Izquierdo, J., 2015. Eastern Boundary Currents off North-West Africa. Currents off NW Africa. IOC-UNESCO.

Pierrot, D., Neill, C., Sullivan, K., Castle, R., Wanninkhof, R., Lüger, H., Johannessen, T., Olsen, A., Feely, R.A., Cosca, C.E., 2009. Recommendations for autonomous underway pCO2 measuring systems and data-reduction routines. Deep Sea Res. 56, 512–522.

Roobaert, A., Laruelle, G.G., Landschützer, P., Gruber, N., Chou, L., Regnier, P., 2019. The spatiotemporal dynamics of the sources and sinks of CO2 in the global coastal ocean. Global Biogeochem. Cycles 33 (12), 1693–1714.

Santana-Casiano, J.M., González-Dávila, M., 2015. Ocean Acidification in the Canary Current Large Marine Ecosystem. Ocean Acidification in the CCLME. IOC-UNESCO.

Santana-Casiano, J.M., González-Dávila, M., Ucha, I.R., 2009. Carbon dioxide fluxes in the Benguela upwelling system during winter and spring: a comparison between 2005 and 2006. Deep Sea Res. Part II Top. Stud. Oceanogr. 56 (8), 533–541.

Sharp, J.D., Pierrot, D., Humphreys, M.P., Epitalon, J.-M., Orr, J.C., Lewis, E.R., Wallace, D.W.R., 2020. CO2SYSv3 for MATLAB. Zenodo. https://doi.org/10.5281/ZENODO.3950563.

Siemer, J.P., Machín, F., González-Vega, A., Arrieta, J.M., Gutiérrez-Guerra, M.A., Pérez-Hernández, M.D., Vélez-Belchí, P., Hernández-Guerra, A., Fraile-Nuez, E., 2021. Recent trends in SST, chl-a, productivity and wind stress in upwelling and open ocean areas in the upper eastern North Atlantic subtropical gyre. J. Geophys. Res.: Oceans 126 (8), e2021JC017268.

Steinhoff, T., Bange, H.W., Kock, A., Wallace, D.W.R., Körtzinger, A., 2012. Biological productivity in the Mauritanian upwelling estimated with a triple gas approach. Biogeosci.Discuss. 2012 4853–4875.

Takahashi, T., Sutherland, S.C., Sweeney, C., Poisson, A., Metzl, N., Tilbrook, B., Bates, N., Wanninkhof, R., Feely, R.A., Sabine, C., 2002. Global sea-air CO2 flux based on climatological surface ocean pCO2, and seasonal biological and temperature effects. Deep Sea Res. 49 (9–10), 1601–1622.

Torres, R., Turner, D., Rutllant, J., Sobarzo, M., Antezana, T., Gonzalez, H.E., 2002. CO2 outgassing off central Chile (31-30degreeS) and northern Chile (24-23degreeS) during austral summer 1997: the effect of wind intensity on the upwelling and ventilation of CO2-rich waters. Deep Sea Res. 49 (8), 1413–1429.

Varela, R., Álvarez, I., Santos, F., deCastro, M., Gómez-Gesteira, M., 2015. Has upwelling strengthened along worldwide coasts over 1982-2010? Sci. Rep. 5 (1), 10016.

Vélez-Belchí, P., Pérez-Hernández, M.D., Casanova-Masjoan, M., Cana, L., Hernández-Guerra, A., 2017. On the seasonal variability of the canary current and the atlantic meridional overturning circulation. J. Geophys. Res.: Oceans 122 (6), 4518–4538.

Wanninkhof, R., 2014. Relationship between wind speed and gas exchange over the ocean revisited. Limnol Oceanogr. Methods 12 (6), 351–362.

Weiss, R.F., 1974. CO2 in water and seawater: the solubility of a non-ideal gas. Mar. Chem. 2, 203–215.

Wentz, F.J.J., Scott, R., Hoffman, M., Leidner, R., Atlas, J.A., 2015. Remote sensing systems cross-calibrated multi-platform (CCMP) 6-hourly ocean vector wind analysis product on 0.25 deg grid. Santa Rosa, C.A. Available online at:. Rem. Sens. Syst. www.remss.com/measurements/ccmp.

Wooster, W.S., 1976. The seasonal upwelling cycle along the eastern boundary of the North Atlantic. J. Mar. Res. 34, 131–141.